PHYSICAL REVIEW E **71**, 056612 (2005)

Discrete quadratic cavity solitons

O. Egorov, U. Peschel, and F. Lederer
Institute of Condensed Matter Theory and Solid State Optics, Friedrich-Schiller-Universität Jena, Max-Wien-Platz 1,
07743 Jena, Germany

(Received 3 February 2005; published 23 May 2005)

We predict the existence of various types of discrete solitons in arrays of coupled optical cavities endowed with a quadratic nonlinearity. We derive mean-field equations and determine their range of validity by comparing results with those from the original round-trip model. By using an analytical approach we identify domains in parameter space where solitons can potentially exist and describe their asymptotic behavior. Taking advantage of these results, we numerically find discrete solitons of different topologies. Some of them are unique to discrete models. Ultimately, we study the stability of these soliton solutions and find that discreteness appreciably influences this behavior.

DOI: 10.1103/PhysRevE.71.056612 PACS number(s): 42.65.Tg, 42.65.Wi, 42.65.Pc, 42.82.Et

I. INTRODUCTION

Discrete systems, such as semiconductor superlattices, molecular chains, waveguide arrays, or coupled pendulums, share many interesting and somehow intriguing features. Recently much progress has been made in experimentally and theoretically studying intrinsic light localization in evanescently coupled waveguide arrays, a prominent example of a discrete system. Light propagation in such arrays exhibits striking anomalies in comparison with beams propagating in usual continuous systems (film waveguides, bulk media). The theoretical predictions of “discrete diffraction” phenomena [1] provided the basis for numerous experimental observations. The particular advantage of “discrete diffraction” is the possibility to be controlled in size and sign by the input conditions [2–5]. Diffractive beam spreading can even be arrested and diverging light can be focused.

Consequently, solitary waves are likewise expected to behave differently in discrete systems compared with continuous ones. In 1988 Christodoulides and Joseph [6] predicted the existence of discrete solitons in waveguide arrays with Kerr nonlinearity. Later this concept was successfully applied to light localization in quadratic waveguide arrays where several additional features have been identified, such as, e.g., the formation of discrete solitons with different topologies compared to the Kerr case [7]. For the limiting case of strong localization analytical soliton solutions were derived [8]. Later, optical domain walls and quasirectangular localized modes were found [9]. Eventually, following these theoretical predictions the existence of discrete solitons has been experimentally verified in both cubic [10] and quadratic waveguide arrays [11].

Up to date most investigations have focused on conservative discrete optical systems. A logical step is to extend these studies to dissipative systems where gain and loss play a significant role. A technologically feasible implementation is a nonlinear waveguide array with dielectric mirrors at the end faces [array of coupled zero-dimensional (0D) Fabry-Pérot resonators] where radiation losses can be compensated for by a driving or pump field.

Over the years a bundle of nonlinear effects has been studied in 1D (film) and 2D (bulk) Fabry-Pérot cavities (continuous system) where canonical diffraction occurs. The simultaneous presence of losses and a driving field has a significant effect on the physics of the system. Moreover, nonlinear effects occur for much less power compared to single pass configurations because of resonant field enhancement in the cavity. But it is well known that the interplay of feedback, loss, gain, and nonlinearity leads to a considerably richer dynamical behavior than that observed in conservative environments. The system can adapt to the driving field in different ways, giving rise to multistability [12], and, as consequences, pattern formation [13–17], and other types of spatial self-organization. In particular, so-called cavity solitons (CSs) may exist on a stable and preferably flat background (for a recent review see [18] and reference therein). They represent localized defects and can either locally increase (bright CSs) or decrease (dark CSs) the transmission of the Fabry-Pérot cavity. Once excited by a local change of the incident field, in principle, they stay forever on a flat holding beam, even if the initial excitation has been switched off. Such robust self-contained localized structures (CSs) were observed in different configurations, namely, in cavities with saturable absorbers [19], in semiconductor microresonators [20,21], in cavities with the Kerr nonlinearity [22], in cavities with a quadratic nonlinearity for both the up- [second-harmonic generation (SHG)] [23,24] and down-conversion cases (optical parametric oscillator) [25–27]. It was found [18] that CSs exist preferably in the vicinity of subcritical bifurcations of the homogeneous solution of the nonlinear system. The concepts of cavity solitons and pattern formation were confirmed experimentally in semiconductor microresonators [28–30].

As suggested above it was only natural to extend these studies to discrete systems. Recently, the existence and properties of discrete cavity solitons were studied in an array of coupled waveguide cavities endowed with the Kerr nonlinearity [31].

In the present paper a detailed theoretical investigation of discrete cavity solitons in quadratic nonlinearities is performed. The first part of the paper is devoted to the derivation of mean-field equations from the more fundamental, but also more cumbersome, round-trip model. Although performed many years ago for continuous systems [13] and very

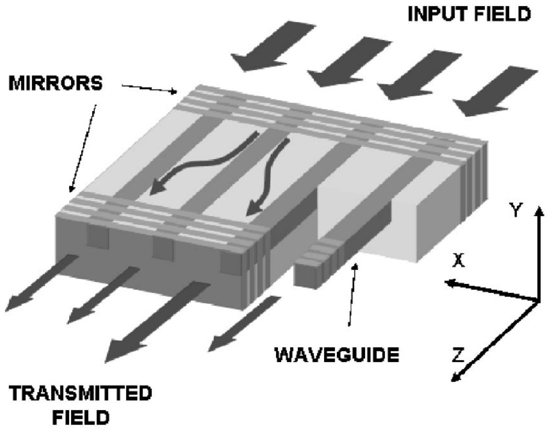

FIG. 1. Array of coupled waveguide cavities with mirrors at the end facets.

concisely for discrete systems with the Kerr nonlinearity [31], it seems to be in order to work out this approximation in detail for the more involved case of quadratic nonlinearities. By using this mean-field model we perform a comprehensive study of the dynamical behavior of this discrete quadratic system. This includes an analysis of the homogeneous nonlinear states (discrete plane waves) and their stability properties, the application of an analytical approach for disclosing the effect of the numerous system parameters on the complex behavior, in particular, the identification of domains in parameter space where discrete cavity solitons (DCSs) of different topologies may exist. Then, we derive numerically various types of quadratic cavity solitons and study their stability. Eventually, we identify the limits of the mean-field model by comparing the results with those obtained by using the round-trip model.

II. MATHEMATICAL MODEL

Here we consider an array of coupled single-mode waveguide cavities endowed with a quadratic nonlinear material and high-finesse dielectric mirrors at the end faces (see Fig. 1) and restrict ourselves to the up-conversion case where radiation losses are compensated for by an external driving field at the fundamental frequency (FF). We assume that the system is doubly resonant for both the FF and the second-harmonic fields and that phase matching is approximately achieved by periodically poling the material [quasi-phase-matching (QPM)]. In addition, the cavities are assumed to be short compared with both the linear coupling length and the nonlinear coherence length and that frequency conversion within a single round trip is small. Hence, all the processes we are looking for, as evanescent coupling or frequency conversion, will evolve upon many round trips and can be regarded as genuine cavity effects.

Basically, we restrict our considerations to a quasi-infinite and homogeneous chain of identical weakly coupled high-Q cavities (Fig. 1). It is well known that mean-field models apply to 1D and 2D high-finesse cavities, no matter whether cubic [13] or quadratic [24] nonlinearities are involved. But it is not evident what these mean-field equations look like in the discrete case and, in particular, how the real cavity parameters are related to the mean-field parameters. To shed some light onto this issue we are going to derive the respective mean-field equations in an array of quadratic cavities, similarly to, but in more detail than, was done for cubic nonlinearities in [31].

We start with the well-known evolution equations for the slowly varying envelopes of the forward u^+, v^+ and backward propagating u^-, v^- field amplitudes in evanescently coupled waveguides, taking into account quadratic nonlinearities [1] as

$$\pm i\frac{\partial u_n^\pm}{\partial z} + \frac{i}{\tilde{V}_F}\frac{\partial u_n^\pm}{\partial t} + c_F(u_{n+1}^\pm + u_{n-1}^\pm) + \chi_{\text{eff}}^{(2)} u_n^{\pm *} v_n^\pm e^{\mp i\Delta\beta z} = 0,$$

$$\pm i\frac{\partial v_n^\pm}{\partial z} + \frac{i}{\tilde{V}_S}\frac{\partial v_n^\pm}{\partial t} + c_S(v_{n+1}^\pm + v_{n-1}^\pm) + \chi_{\text{eff}}^{(2)} u_n^{\pm 2} e^{\pm i\Delta\beta z} = 0, \quad (1)$$

where the real-valued electric field reads as

$$\vec{E}(x,y,z,t) = \sum_n \mathrm{Re}\Bigg(\frac{1}{\sqrt{P_F}} \vec{E}_F(x-x_n,y)[u_n^+(z,t)e^{i\beta_F z} + u_n^-(z,t)e^{-i\beta_F z}]e^{-i\omega_F t} + \frac{1}{\sqrt{P_S}}\vec{E}_S(x-x_n,y) \times [v_n^+(z,t)e^{i\beta_S z} + v_n^-(z,t)e^{-i\beta_S z}]e^{-2i\omega_F t}\Bigg)$$

with $\vec{E}_{F,S}(x,y)$ as the linear mode profiles of the waveguide at fundamental (ω_F) and second-harmonic $(2\omega_F)$ frequencies, respectively, and $P_{F,S} = \frac{1}{4}\int dx\, dy [\vec{E}_{F,S} \times \vec{H}_{F,S}^* + \text{c.c.}] \cdot \vec{e}_z$ as the guided power for the unit amplitudes $u_n^\pm, v_n^\pm = 1$. The slowly varying envelopes are normalized such, that their squared modulus corresponds to the guided power in each waveguide at the respective frequency. The propagation constants $\beta_{F,S}$ of the guided modes determine the group velocities $\tilde{V}_{F,S}$ by their spectral derivatives as $\tilde{V}_{F,S}^{-1} = \partial\beta/\partial\omega|_{\omega=\omega_F,\omega_S}$. They also enter the phase mismatch $\Delta\beta = 2\beta_F - \beta_S + n2\pi/\Lambda$ between FF and SH waves. Here n is an integer and Λ the poling period of the QPM grating. The nonlinear coupling of FF and SH is mediated by a type I interaction, where the corresponding nonlinear coefficient has the form

$$\chi_{\text{eff}}^{(2)} = \frac{\varepsilon_0 \omega_F}{4P_F\sqrt{P_S}} \sum_{i,j,k=1}^{3} \int_{-\infty}^{\infty}\int_{-\infty}^{\infty} \chi_{ijk}^{(2)}(x,y,-\omega_F;2\omega_F,-\omega_F) \times E_{F_i}^*(x,y) E_{F_j}^*(x,y) E_{S_k}(x,y)\, dx\, dy.$$

Because we assume Kleinman symmetry the nonlinear coefficient, which drives SHG, is identical.

The coupling strength between adjacent waveguides separated by Δx is determined by

$$c_{F,S} = \frac{\varepsilon_0 \omega_{F,S}}{4P_{F,S}} \sum_{j,k=1}^{3} \int_{-\infty}^{\infty} \int_{-\infty}^{\infty} \Delta\varepsilon_{jk}(x,y) \times E^{*}_{F,S_j}(x,y) E_{F,S_k}(x-\Delta x,y) dx\, dy .$$

Here $\Delta\varepsilon(x,y)$ represents the change of the dielectric coefficient created by an adjacent guide.

The optical response of the mirrors enters Eqs. (1) as boundary conditions at $z=0,l$ of the form

$$u_n^+(0) = \rho_F e^{i\Phi_F} u_n^-(0) + W_n, \quad u_n^-(l) = \rho_F e^{i\Phi_F} u_n^+(l),$$

$$v_n^+(0) = \rho_S e^{i\Phi_S} v_n^-(0), \quad v_n^-(l) = \rho_S e^{i\Phi_S} v_n^+(l), \tag{2}$$

where the phase $\Phi_{F,S}=\beta_{F,S} l + \varphi_{F,S}$ contains the propagation term $\beta_{F,S} l$ as well as the shift $\varphi_{F,S}$ caused by reflection at the mirrors. For convenience, we assume a symmetric cavity with nonabsorbing mirrors and the amplitude reflection coefficients ρ_F, ρ_S. Each waveguide is excited by the respective driving field W_n, which is given by the overlap of the modal field with the externally applied field as

$$W_n = \frac{T_F}{2P_F} \int_{-\infty}^{\infty} \int_{-\infty}^{\infty} \Big[\vec{E}^{*}(x-x_n,y) \times \vec{H}^{\mathrm{ext}}(x,y,z=0,\omega_F) \Big] \cdot \vec{e}_z \, dx\, dy,$$

where $\vec{H}^{\mathrm{ext}}(x,y,z=0,\omega_F)$ is the transverse component of the complex magnetic field at the entrance facet of the waveguide and T_F the transmission coefficient of the front mirror.

After having performed the Fourier transformation in Eq. (1) with respect to time t and position n as $U_q^{\pm}(\omega,z) = \sum_n \int dt\, u_n^{\pm}(t,z) \exp(i\omega t - iqn)$, we can integrate the remaining ordinary differential equations with respect to the propagation coordinate z. Thus, the amplitudes within the cavity can be expressed by the field amplitude at the output mirror $U_n^{\pm}(\omega;l), V_n^{\pm}(\omega;l)$ as

$$U_q^{\pm}(\omega;z) = U_q^{\pm}(l) e^{\pm i(\omega/\tilde{V}_F + 2c_F \cos q)(z-l)} \mp \frac{i\chi^{(2)}_{\mathrm{eff}}}{2\pi N} \int_z^l dz' e^{\pm i(\omega/\tilde{V}_F + 2c_F \cos q)(z-z')} \int_{-\infty}^{\infty} d\omega' \sum_{q'} U^{*\pm}_{q'-q}(\omega'-\omega;z') V^{\pm}_{q'}(\omega';z') e^{\mp i\Delta\beta z'},$$

$$V_q^{\pm}(\omega;z) = V_q^{\pm}(l) e^{\pm i(\omega/\tilde{V}_S + 2c_S \cos q)(z-l)} \mp \frac{i\chi^{(2)}_{\mathrm{eff}}}{2\pi N} \int_z^l dz' e^{\pm i(\omega/\tilde{V}_S + 2c_S \cos q)(z-z')} \int_{-\infty}^{\infty} d\omega' \sum_{q'} U^{\pm}_{q-q'}(\omega-\omega';z') U^{\pm}_{q'}(\omega';z') e^{\pm i\Delta\beta z'},$$

where the exponential function in the integral represents the Green's function. In a next step we replace the fields in the kernel of the integrals by their values at the boundaries, thus assuming the linear field profile to be maintained in the cavity. Adding the boundary conditions (2) we get in lowest nontrivial order

$$\rho_F e^{i\Phi_F} U_q^-(\omega;0) + W_q = U_q^+(\omega;l) e^{-i(\omega/\tilde{V}_F + 2c_F \cos q)l} - \frac{i\chi^{(2)}_{\mathrm{eff}}}{2\pi N} e^{-i(\omega/\tilde{V}_F + 2c_F \cos q + \Delta\beta)l} \int_{-\infty}^{\infty} d\omega' \sum_{q'} U^{+*}_{q'-q}(\omega'-\omega;l) V^{+}_{q'}(\omega';l) \times \int_0^1 dz' e^{i\{\omega'(1/\tilde{V}_S - 1/\tilde{V}_F) + 2c_S \cos q' - 2c_F[\cos(q'-q) + \cos(\mathrm{q})] - \Delta\beta\}(z'-1)}, \tag{3a}$$

$$U_q^-(\omega;0) = \rho_F U_q^+(\omega;l) e^{i\Phi_F + i(\omega/\tilde{V}_F + 2c_F \cos q)l} + \frac{i\chi^{(2)}_{\mathrm{eff}} \rho_F \rho_S e^{i(\Phi_S - \Phi_F)}}{2\pi N} e^{i(\omega/\tilde{V}_F + 2c_F \cos q + \Delta\beta)l} \int_{-\infty}^{\infty} d\omega' \sum_{q'} U^{+*}_{q'-q}(\omega'-\omega;l) V^{+}_{q'}(\omega';l) \times \int_0^1 dz' e^{-i\{\omega'(1/\tilde{V}_S - 1/\tilde{V}_F) + 2c_S \cos q' - 2c_F[\cos(q'-q) + \cos(\mathrm{q})] - \Delta\beta\}(z'-1)}, \tag{3b}$$

$$\rho_S e^{i\Phi_S} V_q^-(\omega;0) = V_q^+(\omega;l) e^{-i(\omega/\tilde{V}_S + 2c_S \cos q)l} - \frac{i\chi^{(2)}_{\mathrm{eff}}}{2\pi N} e^{-i(\omega/\tilde{V}_S + 2c_S \cos q - \Delta\beta)l} \int_{-\infty}^{\infty} d\omega' \sum_{q'} U^{+}_{q-q'}(\omega-\omega';l) U^{+}_{q'}(\omega';l) \times \int_0^1 dz' e^{i\{\omega(1/\tilde{V}_F - 1/\tilde{V}_S) - 2c_S \cos q + 2c_F[\cos(q-q') + \cos(q')] + \Delta\beta\}(z'-l)}, \tag{4a}$$

$$V_q^-(\omega;0) = \rho_S V_q^+(\omega;l) e^{i\Phi_s + i(\omega/\tilde{V}_S + 2c_S \cos q)l} + \frac{i\chi^{(2)}_{\mathrm{eff}} \rho_F^2 e^{i2\Phi_F}}{2\pi N} e^{i(\omega/\tilde{V}_S + 2c_S \cos q - \Delta\beta)l} \int_{-\infty}^{\infty} d\omega' \sum_{q'} U^{+}_{q-q'}(\omega-\omega';l) U^{+}_{q'}(\omega';l) \times \int_0^l dz' e^{-i\{\omega(1/\tilde{V}_F - 1/\tilde{V}_S) - 2c_S \cos q + 2c_F[\cos(q-q') + \cos(q')] + \Delta\beta\}(z'-1)}, \tag{4b}$$

where the boundary conditions have been used to replace $U_q^-(\omega;l), U^-_{q'-q}(\omega'-\omega;l)$, and $V^-_{q'}(\omega';l)$ in Eqs. (3b) and (4b). Next, we carry out the integration over z' in Eqs. (3) and (4). Assuming that temporal walk-off and "discrete diffraction" only marginally effect the nonlinear interaction during a single passage we neglect the terms with $\widetilde{V}_{F,S}, c_{F,S}$ in the exponent of the nonlinear parts. Then, Eqs. (3b) and (4b) are subtracted from Eqs. (3a) and (4a), respectively. This leads to expressions containing only the forward propagating fields $U_q^+(\omega), V_q^+(\omega)$ at $z=l$:

$$U_q^+(\omega)e^{i\Delta\Phi_F}\Big[e^{-i\Delta\Phi_F-i(\omega/\widetilde{V}_F+2c_F\cos q)l}-\rho_F^2 e^{i\Delta\Phi_F+i(\omega/\widetilde{V}_F+2c_F\cos q)l}\Big]-W_q$$
$$=\frac{i\chi_{\text{eff}}^{(2)}}{2\pi N}\operatorname{sinc}\left(\frac{\Delta\beta l}{2}\right)\left(\rho_F^2\rho_S e^{i\Delta\Phi_S}e^{i\Delta\beta l/2}+e^{i\Delta\beta l/2}\right)l\int_{-\infty}^{\infty}d\omega'\sum_{q'}U_{q'-q}^{+*}(\omega'-\omega)V_{q'}^+(\omega'),$$

$$V_q^+(\omega)e^{i\Delta\Phi_S}\Big[e^{-i\Delta\Phi_S-i(\omega/\widetilde{V}_S+2c_S\cos q)l}-\rho_S^2 e^{i\Delta\Phi_S+i(\omega/\widetilde{V}_S+2c_S\cos q)l}\Big]$$
$$=\frac{i\chi_{\text{eff}}^{(2)}}{2\pi N}\operatorname{sinc}\left(\frac{\Delta\beta l}{2}\right)\left(\rho_F^2\rho_S e^{i(\Delta\Phi_S+2\Delta\Phi_S)}e^{i\Delta\beta l/2}+e^{i\Delta\beta l/2}\right)l\int_{-\infty}^{\infty}d\omega'\sum_{q'}U_{q-q'}^{+}(\omega-\omega')U_{q'}^+(\omega'), \tag{5}$$

where $\Delta\Phi_{F,S}=\Phi_{F,S}-\beta_{F,S}^{\text{res}}$ is the respective detuning from the nearest cavity resonance $2\beta_{F,S}^{\text{res}}l=2\pi m$ $(m=1,2,\ldots)$. As usual the mean-field model holds only near a longitudinal cavity resonance $\Delta\Phi_{F,S}\ll 2\pi$ and walk-off, frequency conversion, and coupling have to be small for a single passage $(\omega l/\widetilde{V}_{F,S}\ll 1, c_{F,S}l\ll 1)$. Hence, the exponentials on the right-hand side of Eq. (5) are close to unity and can be linearized. It is worth to note that we intentionally extract the phase term from the square brackets of Eq. (5) for the sake of minimization of higher-order errors throughout the Taylor expansion. As a preliminary result we obtain a set of mean-field equations in Fourier space:

$$-i(1-\rho_F^2)\Big[\omega\widetilde{V}_F^{-1}l+2c_F l\cos q+\Delta\Phi_F\Big]U_q^+(\omega)$$
$$+(1-\rho_F^2)U_q^+(\omega)-W_q$$
$$=\frac{i\chi_{\text{eff}}^{(2)}}{2\pi N}\operatorname{sinc}\left(\frac{\Delta\beta l}{2}\right)\Big(\rho_F^2\rho_S e^{i\Delta\beta l/2}$$
$$+e^{-i\Delta\beta l/2}\Big)l\int_{-\infty}^{\infty}d\omega'\sum_{q'}U_{q'-q}^{+*}(\omega'-\omega)V_{q'}^+(\omega'),$$

$$-i(1-\rho_S^2)\Big[\omega\widetilde{V}_S^{-1}l+2c_S l\cos q+\Delta\Phi_S\Big]V_q^+(\omega)+(1-\rho_S^2)V_q^+(\omega)$$
$$=\frac{i\chi_{\text{eff}}^{(2)}}{2\pi N}\operatorname{sinc}\left(\frac{\Delta\beta l}{2}\right)\left(\rho_F^2\rho_S e^{-i\Delta\beta l/2}+e^{i\Delta\beta l/2}\right)l$$
$$\times\int_{-\infty}^{\infty}d\omega'\sum_{q'}U_{q-q'}^{+}(\omega-\omega')U_{q'}^+(\omega').$$

After having performed the inverse Fourier transformations the appropriately scaled evolution equations for the slowly varying envelope of the transmitted FF (u_n) and the SH field (v_n) in the nth waveguide read as

$$i\frac{\partial u_n}{\partial T}+C_1(u_{n-1}+u_{n+1})-2C_1u_n+(i+\Delta_1)u_n+u_n^*v_n=E,$$

$$i\frac{\partial v_n}{\partial T}+C_2(v_{n-1}+v_{n+1})-2C_2v_n+(i\delta+\Delta_2)v_n+u_n^2=0, \tag{6}$$

where the evolution time T is scaled to the FF photon lifetime $\tau_{\text{ph}}=[(1+\rho_F^2)/(1-\rho_F^2)]l\widetilde{V}_F^{-1}$. The system (6) is the set of mean-field equations describing the field dynamics in an array of coupled quadratic cavities.

The cavity parameters are related to the mean-field parameters as follows. The detunings of both fields from the respective cavity resonances read as

$$\Delta_1=-\frac{(1+\rho_F^2)}{(1-\rho_F^2)}\Delta\Phi_F+2C_1,\quad \Delta_2=-\frac{\widetilde{V}_S(1+\rho_F^2)}{\widetilde{V}_F(1-\rho_F^2)}\Delta\Phi_S+2C_2,$$

the ratio of the radiation losses δ is determined by the ratio of the FF to SH photon lifetimes as $\delta=[\widetilde{V}_S(1-\rho_S^2)/\widetilde{V}_F(1+\rho_S^2)]/[(1-\rho_F^2)/(1+\rho_F^2)]$. The normalized coupling strengths are related to the coupling constants as $C_1=\widetilde{V}_F\tau_{\text{ph}}c_F$, $C_2=\widetilde{V}_S\tau_{\text{ph}}c_S$ and the normalized optical field amplitudes are given by

$$u_n=\chi_{\text{eff}}^{(2)}l\operatorname{sinc}\left(\frac{\Delta\beta l}{2}\right)\frac{\left|\rho_F^2\rho_S e^{-i\Delta\beta l/2}+e^{i\Delta\beta l/2}\right|}{(1-\rho_F^2)}\sqrt{\frac{\widetilde{V}_S(1+\rho_F^2)}{\widetilde{V}_F(1+\rho_S^2)}}u_n^+,$$

$$v_n=\chi_{\text{eff}}^{(2)}l\operatorname{sinc}\left(\frac{\Delta\beta l}{2}\right)\frac{\left(\rho_F^2\rho_S e^{i\Delta\beta l/2}+e^{-i\Delta\beta l/2}\right)}{(1-\rho_F^2)}v_n^+,$$

$$E=i\frac{\left|\rho_F^2\rho_S e^{-i\Delta\beta l/2}+e^{i\Delta\beta l/2}\right|}{(1-\rho_F^2)^2}\sqrt{\frac{\widetilde{V}_S(1+\rho_F^2)}{\widetilde{V}_F(1+\rho_S^2)}}lW_n. \tag{7}$$

In experimental setups the SH field is usually much more confined in the transverse direction than the FF field [11]; thus, the coupling is much less and can be neglected ($C_2=0$). As a consequence stationary solutions of the system (6) simplify considerably because the SH field can be expressed by the FF one as $v_n = -u_n^2/(i\delta+\Delta_2)$ and only the FF components appear in the final set of equations as

$$(i+\Delta_1)u_n - \frac{1}{i\delta+\Delta_2}|u_n|^2 u_n + C_1(u_{n-1}+u_{n+1}) - 2C_1 u_n = E. \tag{8}$$

Evidently, in the stationary limit the quadratic nonlinearity is mimicked by a complex-valued cubic one. Therefore stationary solutions will be similar to those derived in [31] provided that SH losses are small ($\delta \approx 0$). However, this simplification does not hold for the full dynamical solutions. Hence, typical effects of the quadratic nonlinearity will mainly show up when the field evolution and the stability behavior of stationary solutions are under investigation.

III. PLANE WAVE SOLUTIONS AND THEIR STABILITY

The simplest solution of Eq. (6) is the transversally homogeneous state where all cavities are equally excited. Except for modifying the stability behavior, the coupling has no effect in this case. This homogeneous or plane wave (PW) solution is determined by the properties of the isolated cavity. However, PW solutions play a key role with regard to the existence and stability of DCSs, which are localized objects on a homogeneous background. A stable DCS requires the stability of the underlying PW background. Moreover, the so-called critical points in parameter space where PW solutions destabilize are potential bifurcation points for DCSs. Therefore, the investigation of PW solutions and their stability properties is a prerequisite for the identification of DCSs.

The intensities of the stationary PW solutions ($|u_n|^2 = |b_1|^2$ for the FF and $|v_n|^2 = |b_2|^2$ for the SH of Eq. (6) are [12,16]

$$\begin{aligned}[]&[|b_1|^4 + 2(\delta - \Delta_1\Delta_2)|b_1|^2 + (\Delta_1^2+1)(\Delta_2^2+\delta^2)]|b_1|^2 \\ &\quad = (\Delta_2^2+\delta^2)E^2, \quad |b_2|\sqrt{\Delta_2^2+\delta^2} = |b_1|^2. \end{aligned}\tag{9}$$

The formation of DCSs is closely related to the existence of bistable solutions of Eq. (9), which is realized, provided that

$$\frac{|\Delta_2|(|\Delta_1| - \sqrt{3})}{\sqrt{3}|\Delta_1| + 1} > \delta, \quad \Delta_1\Delta_2 > 0, \tag{10}$$

holds. Thus, for PW bistability the fundamental detuning Δ_1 has to exceed the critical value of $\sqrt{3}$ and the signs of FF and SH detunings have to coincide (Fig. 2).

Having found the PW solutions they have to be probed against stability. In what follows we combine the usual linear stability analysis with the search for asymptotic solutions, which resemble the linear limit of soliton tails. The latter issue is of particular importance because we can easily identify domains in parameter space where various kinds of soliton solutions are expected to exist. To tackle both tasks we use a unified mathematical approach in looking for solutions to (6) close to PW background as

$$\begin{aligned}(u_n, v_n, u_n^*, v_n^*) &= (b_1, b_2, b_1^*, b_2^*) + (a_1, a_2, a_1^*, a_2^*) \\ &\quad \times \exp[(\lambda' + i\lambda'')T + (\alpha + i\beta)n]. \end{aligned}\tag{11}$$

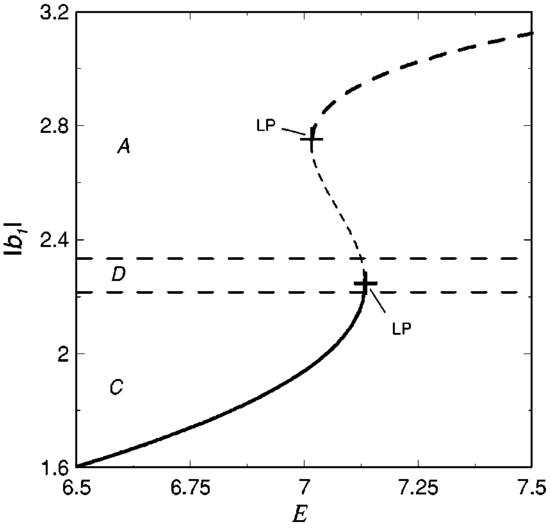

FIG. 2. FF amplitude of PW solutions vs the driving field amplitude E. Solid line, stable; thin dashed line, homogeneously unstable; thick dashed line, modulationally unstable. The horizontal dashed lines divide PW solutions into three parts with different asymptotic behavior. LPs designate the limiting points of bistability. ($C_1 = 0.5, \Delta_1 = -5, \Delta_2 = -2, \delta = 0.6$.)

According to this ansatz linear perturbations can spatially grow or decay ($\alpha \neq 0$) or oscillate ($\beta \neq 0$). Linearizing the evolution equations (6) around the PW solution (b_1, b_2, b_1^*, b_2^*) with respect to the perturbation amplitudes (a_1, a_2, a_1^*, a_2^*) we obtain

$$\begin{aligned}&(\Gamma' + i\Gamma'')a_1 + i\left(\delta_1 + \frac{2|b_1|^2\delta_2}{\delta_2{}^2 + (\Delta_2^-)^2}\right)a_1 + \left(\Delta_1^- - \frac{2|b_1|^2\Delta_2^-}{\delta_2{}^2 + (\Delta_2^-)^2}\right)a_1 \\ &\quad + \left(\frac{i\delta - \Delta_2}{\delta^2 + \Delta_2{}^2}\right)b_1{}^2 a_1^* = 0, \\[1em] &(\Gamma' + i\Gamma'')a_1^* - i\left(\delta_1 + \frac{2|b_1|^2\delta_2}{\delta_2{}^2 + (\Delta_2^+)^2}\right)a_1^* + \left(\Delta_1^+ - \frac{2|b_1|^2\Delta_2^+}{\delta_2{}^2 + (\Delta_2^+)^2}\right)a_1^* \\ &\quad + \left(\frac{-i\delta - \Delta_2}{\delta^2 + \Delta_2{}^2}\right)b_1^{*2} a_1 = 0, \end{aligned}\tag{12}$$

where we have introduced effective losses $\delta_1 = 1 + \lambda'$ and $\delta_2 = \delta + \lambda'$, detunings $\Delta_{1,2}^{\pm} = \Delta_{1,2} \pm \lambda''$, and discrete diffraction coefficients $\Gamma' = 2C_1(\cosh\alpha\cos\beta - 1)$ and $\Gamma'' = 2C_1 \sinh\alpha \sin\beta$.

From Eq. (12) we can extract information about the existence and stability of asymptotically increasing or decreasing and periodic solutions.

First we deal with the usual PW stability issue by setting $\alpha = 0$. The solution is stable (decaying perturbation) for $\lambda' < 0$, and unstable (growing perturbation) for $\lambda' > 0$. Critical points in parameter space are marked by a stability transition at $\lambda' = 0$. Depending on the spatial modulation β of the perturbation and on the imaginary part λ'' of the respective eigenvalue at the critical points ($\lambda' = 0$), we may distinguish between homogeneous instability for $\beta = 0$ and modulational

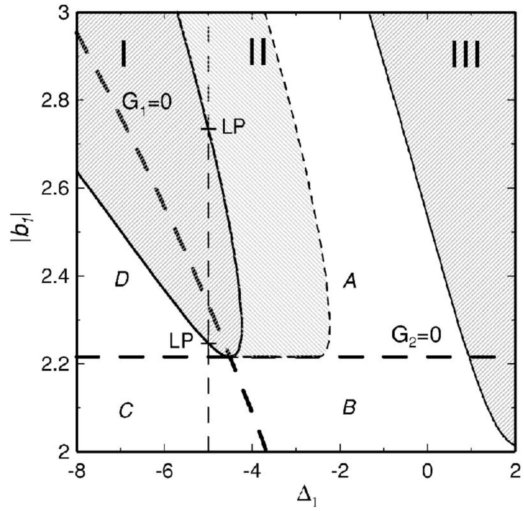

FIG. 3. Domains of stable and unstable discrete PW solutions in parameter space defined by the FF detuning Δ_1 and the FF amplitude $|b_1|$. Instability domains are shaded [homogeneous (I), modulational (II), and Hopf (III) instability]. The vertical dashed line corresponds to the curve in Fig. 2. Thick dashed lines designate the change in sign of G_1 and G_2 [Eqs. (15), whereas these signs stay unchanged within domains A, B, C, and D. ($C_1=0.5, \Delta_2=-2, \delta=0.6$.)

instability (MI) for $\beta \neq 0$. The growth of the instability may be purely exponential ($\lambda''=0$) or oscillating ($\lambda'' \neq 0$, Hopf bifurcation).

From the derived stability criteria we can now distinguish between different domains in parameter space, which are plotted in Fig. 3. In domain I the PW solution is trivially unstable. It corresponds to the middle branch of the hysteresis loop (Fig. 2) and is confined by the limiting points (LPs) of bistability following from Eq. (9) as

$$|b_1|^2_{\mathrm{LP}} = \frac{1}{3}[2(\delta - \Delta_1\Delta_2) \pm \sqrt{4(\delta - \Delta_1\Delta_2)^2 - 3(\Delta_1^2+1)(\Delta_2^2+\delta)}]. \tag{13}$$

PW solutions in domains II and III are subject to modulational or Hopf instability, respectively. Both domains will be dealt with below. It is worth noting that a certain driving field amplitude E corresponds to multiple values for the FF PW solution $|b_1|$. Thus, it is convenient to use the PW amplitude as a parameter rather than E, which easily follows from Eq. (9).

IV. ASYMPTOTIC BEHAVIOR

As was discussed in the previous section, the first necessary condition for the existence of spatially localized solutions, i.e., cavity solitons, is a stable PW background. Obviously, the soliton tails have to converge to the PW background far from the soliton center. Therefore, the second evident condition is the existence of spatially increasing and decreasing solutions around the PWs. A linear theory for the description of the soliton tails can be applied, provided that the amplitude does not deviate too much from the PW background. According to this approximation the tails decrease exponentially as $e^{\pm(\alpha+i\beta)n}$. Therefore, a localized solution can exist only if the real part of the exponent is nonzero ($\alpha \neq 0$). Furthermore the imaginary part β determines the type of DCS, since for $\beta \neq 0$ we observe spatially oscillating tails.

The solvability conditions of Eq. (12) and requiring stationarity ($\lambda'=0, \lambda''=0$) yield the characteristic equation

$$\cosh\alpha \cos\beta - 1 + i \sinh\alpha \sin\beta = \left(G_1 \pm \sqrt{G_2}\right)/2C_1 \tag{14}$$

with

$$G_1 = -\Delta_1 + \frac{2|b_1|^2\Delta_2}{\delta^2+\Delta_2^2}, \quad G_2 = \frac{|b_1|^4}{\delta^2+\Delta_2^2} - \left(1 + \frac{2\delta|b_1|^2}{\delta^2+\Delta_2^2}\right)^2. \tag{15}$$

Depending on the functions G_1 and G_2, Eq. (14) exhibits different types of solutions. The lines in parameter space where G_1 and G_2 change their signs are indicated in Fig. 3. These lines divide the parameter space $[|b_1|, \Delta_1]$ into four regions, namely, the domains $A, G_1 < 0, G_2 > 0$; $B, G_1 < 0, G_2 < 0$; $C, G_1 > 0, G_2 < 0$; and $D, G_1 > 0, G_2 > 0$.

To analyze the set of possible asymptotic solutions of Eqs. (14) and (15) we consider separately these four parameter domains.

In parameter domain A ($G_1 < 0, G_2 > 0$) a possible solution of Eq. (14) is

$$\alpha = 0, \quad \beta = \arccos\left(1 + \frac{1}{2C_1}\left(G_1 \pm \sqrt{G_2}\right)\right). \tag{16}$$

Thus, the small amplitude solutions are purely oscillating ($\beta \neq 0$) and do not increase or decrease in transverse directions. At least one of the solutions (16) is real valued, provided that the system parameters satisfy the inequality

$$4C_1 \geqslant -G_1(|b_1|, \Delta_1) - \sqrt{G_2(|b_1|, \Delta_1)}. \tag{17}$$

At each parameter point where the inequality (17) holds a spatially modulated perturbation with the corresponding wave vector β is stationary. Hence, it is neither growing nor decaying, but just on the verge of destabilization. Hence, if the PW background allows for a solution of the form (16), it is modulationally unstable. Therefore, the inequality (17) marks the right boundary of domain II (see Fig. 3). This boundary [sign of equality in Eq. (17)] coincides exactly with the limiting point of bistability (13) for weak coupling ($C_1=0$). It is interesting to note that the asymptotic solution becomes always staggered ($\beta=\pi$; opposite sign of amplitudes in adjacent waveguides) on the boundary of this domain.

A typical multistable plane wave response is shown in Fig. 2. The modulational instability of the upper plane wave branch (domain A) leads to the formation of a periodic pattern with a spatial period determined by β. Provided that the pump amplitude allows for a second stable PW background (multivalued solution in Fig. 2 between LPs) one cell of it can be extracted to form a bright DCS on the stable low-amplitude background (domain C in Figs. 2 and 3). This case will be considered in the following section.

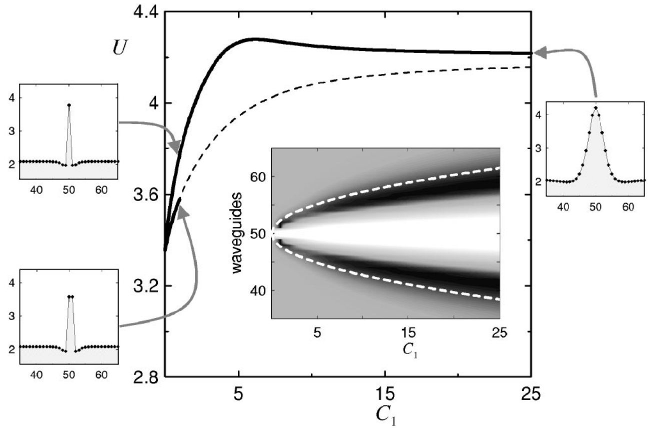

FIG. 4. Maximum FF amplitude of odd and even DCSs vs the coupling constant (dashed line, unstable solutions). The insets show selected DCS profiles and the dependence of the width of odd DCSs on the coupling constant [contour diagram, numerical solution; white dashed line, analytical evaluation (21)]. Parameters: $E=9$, $\Delta_1=-6, \Delta_2=-2, \delta=0.6$.

V. DISCRETE CAVITY SOLITONS

A. Bright solitons

The scaled coupling constant C_1 depends on the waveguide spacing as well as on the mirror reflectivities and can be varied in a wide range. In the "quasicontinuous" limit (strong coupling) Eq. (6) reproduces the effects known from conventional planar cavities, such as, for example, translational symmetry. On the contrary effects of discreteness dominate if the coupling tends to vanish, which can be achieved by increasing the distance between the cavities. In this so-called "anticontinuous" limit the individual cavities are virtually isolated. For vanishing coupling each cavity is not affected by its neighbors. In this trivial case the solitons are constructed by a combination of amplitudes in the isolated cavities, which assume one of three stationary states provided that the response of the isolated cavity is multivalued (Fig. 4 for $C_1 \to 0$). For example, "odd" ("even") DCSs are localized states where one (two) cavity is switched to a high stable level on a low-level background. Increasing the coupling strength the adjacent cavities get involved in the power exchange. The "trivial" localized solution becomes wider and nonlinear effects compensate for the transversal spreading due to discrete diffraction. Because the focusing environment is preferable for bright localized structures, we consider first a negative SH detuning from the cavity resonance ($\Delta_2 < 0$). This choice is evident from Eq. (8) because a specific SH detuning results in either an effective focusing ($\Delta_2 < 0$) or defocusing ($\Delta_2 > 0$) behavior [16,24]. Usually effective focusing allows one to find bright solitons for any coupling strength up to the quasicontinuous limit (Fig. 4 for $C_1 \to \infty$). As expected the difference between odd and even solitons disappears for the very strong coupling.

The lower branch of the plane wave solution in Fig. 2 is a typical background for DCSs considered here. It corresponds to domains C and D in Fig. 3. The soliton tails have to fit the asymptotic solutions around its background. Solving the characteristic equations (14) for both domains we can conclude that the background allows for spatially exponentially increasing (decreasing) solutions. The corresponding coefficients can be obtained easily in domain D as

$$\alpha^{\pm} = \operatorname{arccosh}\left[1 + \left(G_1 \pm \sqrt{G_2}\right)/2C_1\right], \quad \beta = 0. \tag{18}$$

By contrast, asymptotic stationary solutions are slightly oscillating in domain C:

$$\alpha \geqslant \operatorname{arccosh}(1 + G_1/2C_1),$$

$$\beta \leqslant \arcsin\left[\sqrt{-G_2}/\sqrt{G_1(G_1+4C_1)}\right]. \tag{19}$$

It is clear from Eq. (19) that close to the line $G_2(|b_1|,\Delta_1) = 0$ the length of the corresponding spatial oscillations grows to infinity. Moreover the ratio β/α is very small and increases considerably only close to the boundary with domain $B[G_1(|b_1|,\Delta_1)=0$ in Fig. 3]. Therefore DCSs possess monotonically decreasing tails without or with only slight spatial oscillations in domains C and D.

The asymptotic solutions contain information about typical scales of spatial inhomogeneities of the localized structure. Therefore the typical extension of the DCS can be analytically evaluated. Evidently, this method fails for the evaluation of the soliton half-width, because the genuine nonlinear solution is required. But usually it is more important to know the minimal width the soliton requires to exist without interacting with its counterparts. It is clear that this "soliton diameter" exceeds the soliton half-width. Thus, this width can be roughly estimated in requiring that the tails have decreased to about 10% of the peak amplitude giving the number of waveguides d as

$$d = 2 \ln 10/\alpha. \tag{20}$$

Now we use Eqs. (18) and (19) to apply this formula in domains C and D and get for sufficiently large coupling (and $G_1 \gg \sqrt{G_2}$ for domain D):

$$d \approx 6.51\sqrt{C_1/G_1}. \tag{21}$$

Actually this approximation describes surprisingly well the DCS width for any coupling constant except a small domain close to the anticontinuous limit ($C_1 \to 0$) (see white dashed line in inset of Fig. 4).

We start with a detailed discussion of the usually stable odd DCS and will come back to even DCSs below. A typical profile of an odd stable bright DCS (domain D) is displayed in Fig. 5. The shaded part corresponds to the analytically estimated width [Eq. (21)]. The amplitude of soliton tails deviates only slightly from the PW background and can be therefore approximated by our analytical model (in domain D) as

$$U_n^{\pm} = \left[i a_{\pm} \sqrt{(\delta + i\Delta_2)\left(1 + \frac{2\delta|b_1|^2}{\delta^2+\Delta_2^2} \pm i\sqrt{G_2}\right)} \times \exp(\alpha^{\pm} n) + |b_1| \right] e^{i\varphi_b} \tag{22}$$

where $b_1 = |b_1| e^{i\varphi_b}$ is the FF plane wave background and $a_{\pm}$ are arbitrary real amplitudes which determine the contribu-

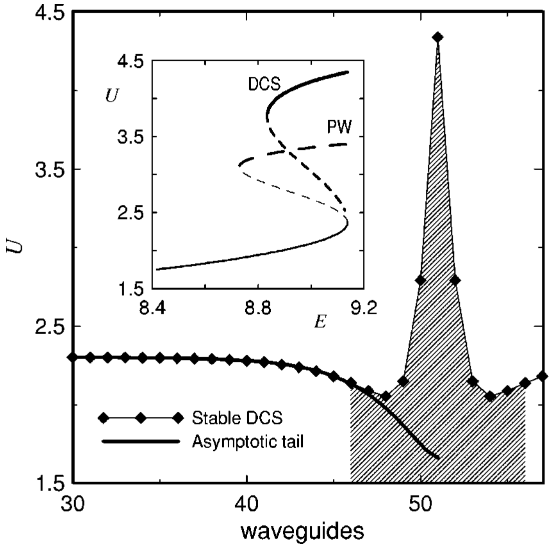

FIG. 5. FF field profile of a typical bright DCS with the corresponding analytical approximation for the tails for $E=9.13$. The shaded area designates the effective soliton width obtained analytically. Inset: FF amplitude of PW solution and maximum FF amplitude of bright DCS vs the pump amplitude E. Dashed lines correspond to homogeneously (thin) and modulationally (thick) unstable states. $(C_1=4, \Delta_1=-6, \Delta_2=-2, \delta=0.6.)$

tion of independent exponential solutions with α^+ and α^- [see Eq. (18)]. Figure 5 displays the agreement between the tails of the genuine DCS and the asymptotic approximation.

Usually, cavity solitons exist on branches in parameter space, which bifurcate from PW branches [18,24]. Indeed, as plotted in the inset of Fig. 5, bright DCSs bifurcate subcritically from the limiting point of PW bistability and stabilize behind the turning point of the respective branch. For there is no appropriate background, no DCS can be found beyond the PW bistability limiting point.

It is interesting to look at the difference of stable and unstable DCSs for driving field E close to the bifurcation point (right LP in inset of Fig. 5). Solving Eq. (18) provides that $\alpha^- \to 0$ close to LP. Therefore, according to Eq. (20) the localized solution becomes flat in the bifurcation point: $d \to \infty$. This explains intuitively the bifurcation of DCS branches from PW solutions in the LP. Thus the approximation (21) fails in this case and the width of stable DCSs is determined by α^+. Hence, the occurrence of two soliton tails with different spatial decay rates reflects the coexistence of stable and unstable solitons being both situated at the soliton hysteresis curve.

Detailed studies show that the size of the bright DCS existence domain increases considerably with negative cavity detuning Δ_1.

B. Soliton with oscillating tails

The quadratic DCSs discussed up to now existed in domains of parameter space where PW bistability takes place. To find out whether DCSs may also exist without an underlying PW bistability we are now going to search for DCS solutions in domain B.

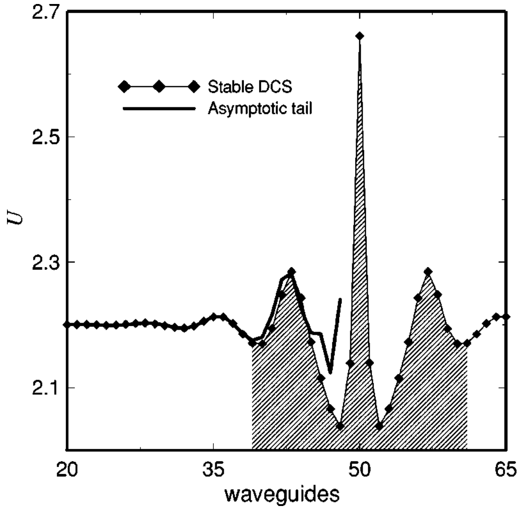

FIG. 6. FF field profile of a stable first-order DCS with oscillating tails. The shaded area designates the effective soliton width. The thick solid line corresponds to the analytical approximation of the soliton tails. $(E=5.3635, C_1=0.75, \Delta_1=-4, \Delta_2=-2, \delta=0.6.)$

Some peculiarities of this particular DCS type can be again understood by taking advantage of the asymptotic analysis. As mentioned before the DCS tails exhibit an oscillating behavior near the boundary to domain B [$G_1 \to 0$ in Eq. (19)]. A typical DCS profile in domain B is displayed in Fig. 6. According to our analysis the exponents of asymptotic solutions satisfy

$$\cosh\alpha\cos\beta = 1 + G_1/2C_1, \quad \sinh\alpha\sin\beta = \pm\sqrt{-G_2}/2C_1, \tag{23}$$

requiring $\alpha \neq 0$ and $\beta \neq 0$. Thus, the DCSs exhibit oscillating tails, which can be approximated as

$$U_n = A_1 \exp[(\alpha + i\beta)n] + A_2 \exp[(\alpha - i\beta)n], \tag{24}$$

where A_1 is an arbitrary complex amplitude and A_2 is determined by

$$A_2 = A_1^* \frac{(\delta - i\Delta_2)}{b_1^{*2}} \{\sqrt{-G_2} + [1 + 2|b_1|^2 \delta/(\delta^2 + \Delta_2^2)]\}.$$

By varying A_1 one can fit the tail (24) to the numerically calculated soliton tail (thick solid line in Fig. 6). Equation (20) approximates the soliton width shown by the shaded area. The oscillating tails suggest that bound states of DCSs can be formed. Therefore, it is no surprise that the respective soliton branches are multistable (see Fig. 7), where every higher-order soliton represents a new bound state with an additional hump. The oscillation period of the tails and, thus, the distance between peaks can be approximated as $P = \pi/\beta$. The highest-order bound state is an infinite periodic pattern which connects the DCS branch with the modulationally unstable domain (vertical line in Fig. 7). Hence, the stable background close to the MI domain can coincide with a stable periodic pattern. It is evident from Fig. 7 that the existence domain of bright DCSs increases with decreasing coupling constant.

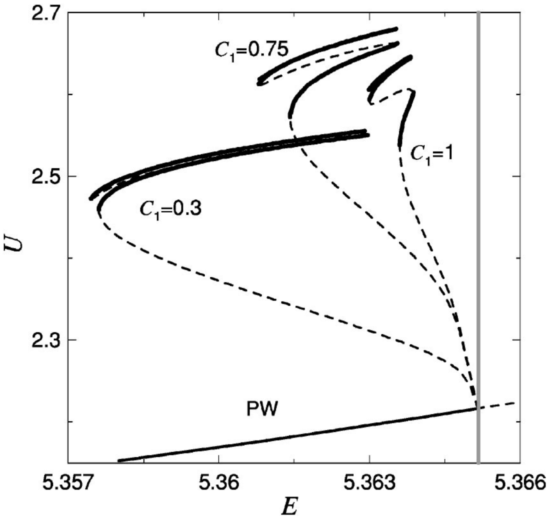

FIG. 7. Maximum amplitude of the FF component of bright DCSs with oscillating tails vs the holding beam E for different coupling constants ($\Delta_1=-4, \Delta_2=-2, \delta=0.6$).

C. Dark staggered solitons

Now we proceed to inspect the upper PW branch, which is displayed in Fig. 2, and belongs to domain A in Fig. 3. For negative detunings this branch is modulationally unstable beyond the limiting point. According to Eq. (17) the size of the instability domain increases with the coupling constant C_1, shown in Fig. 8 by dashed lines. We have shown before that in this parameter domain spatially periodic solutions (16) exist excluding the formation of DCSs. However, it turns out that outside the MI domain (domain A at the right side of the MI in Fig. 3) there are only asymptotically decreasing or increasing solutions of Eq. (14) which read as

$$\alpha^{\pm} = \operatorname{arcosh}\left(-1 + \frac{1}{2C_1}(-G_1 \mp \sqrt{G_2})\right), \quad \beta = \pi. \quad (25)$$

The corresponding small-amplitude distribution $U_n^{\pm}$ is given by Eq. (22) with the exponent $\alpha^{\pm}n + i\pi n$ and $\alpha^{\pm}$ from Eq. (25).

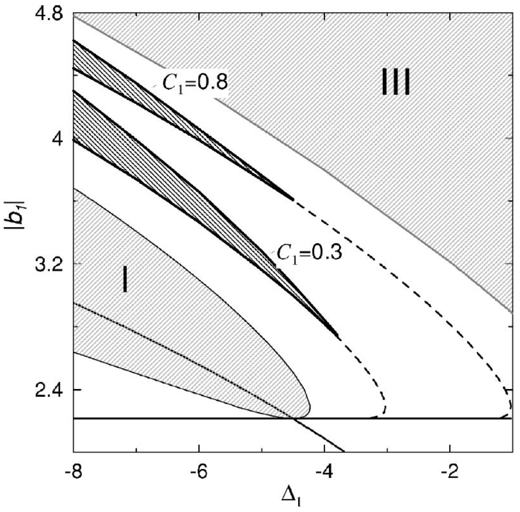

FIG. 8. Existence domain of dark DCS in the parameter plane of FF detuning Δ_1 and FF amplitude $|b_1|$ for different coupling constants C_1 (shaded black areas confined by solid thick lines). The dashed lines are boundaries of modulational instabilities for the corresponding coupling. The PW background is homogenous and Hopf unstable in I and III, respectively (as in Fig. 3). Parameters: $\Delta_2=-2, \delta=0.6$.

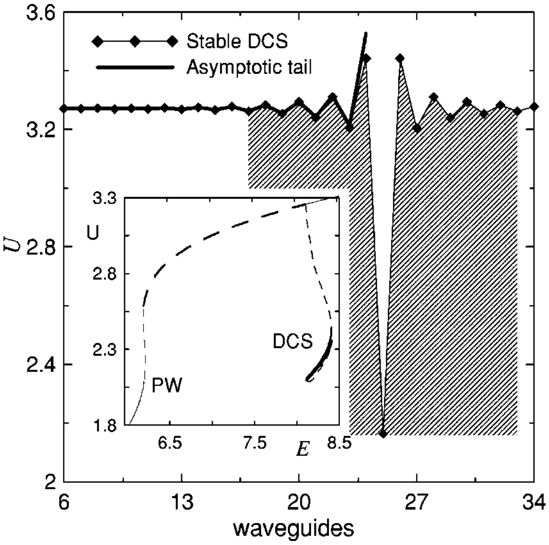

FIG. 9. Profile of dark DCS and the corresponding analytic approximation of the tails for $E=8.2$. Inset: FF amplitude of PW solutions and minimum amplitude of dark discrete cavity soliton branch vs pump amplitude E. Dashed lines correspond to unstable states. ($C_1=0.5, \Delta_1=-4.5, \Delta_2=-2, \delta=0.6$.)

Accordingly, we found a dark DCS branch bifurcating subcritically from the critical point at the termination of the MI domain (DCS branch in the inset of Fig. 9). The stable part of this branch can either terminate exactly at the point of MI or turn back to form a multistable dark soliton branch. The first case is typical for large negative cavity detuning, where the oscillating solution (16) destroys the background in the MI point. The second case occurs near nascent PW bistability (relatively small negative detuning) and higher-order solitons have several intensity dips. The asymptotic DCS tails $U_n^{\pm}$ exhibit a phase difference π between adjacent waveguides (staggered solution), which is a signature for discrete systems. Together with the PW background the soliton tails look sawtoothlike. The asymptotic behavior of the tails is determined by the linear combination of the two solutions (25). It can be seen in Fig. 9 that far from the soliton center the analytic solution (25) coincides exactly with the tails of the numerically determined dark soliton. Equation (20) gives again the dark soliton width shown as the shaded area in Fig. 9. Close to the bifurcation point we have $\alpha^{-} \rightarrow 0$, and hence the unstable dark DCS transforms into the staggered PW solution at the onset of MI.

It is interesting to note that this dark DCS branch has no connection with the bistable domain of the PW hysteresis curve (inset of Fig. 9). The hysteresis curve of the dark DCS is usually several times larger in parameter space than the corresponding PW bistability domain. On increasing the coupling constant, the existence domain of the dark DCS moves

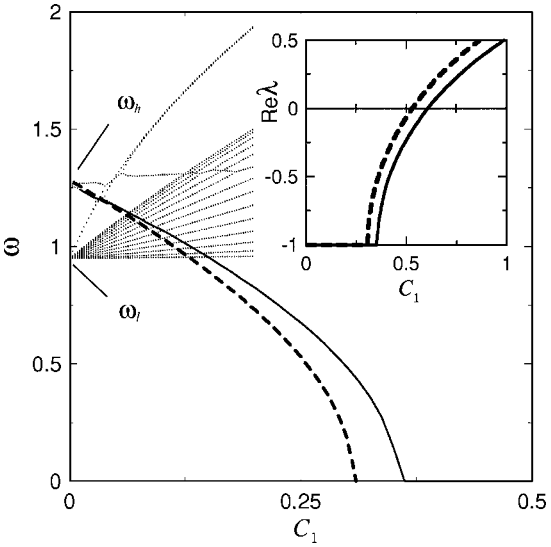

FIG. 10. The imaginary and real parts (in inset) of the eigenvalue of the linear mode for an even DCS vs the coupling constant. ($E=11.2, \Delta_1=-5, \Delta_2=-6, \delta=1$.) The dashed solid line is the analytical approximation.

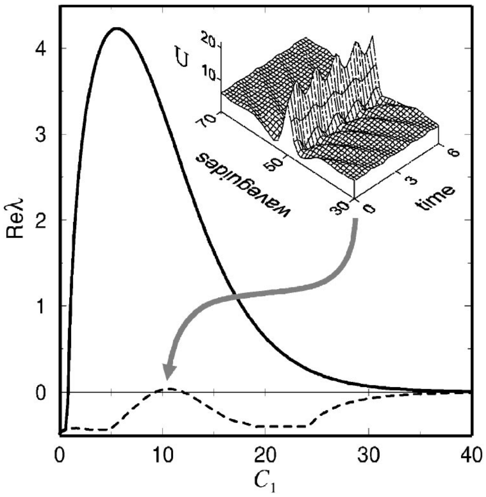

FIG. 11. The maximal growth rate of the linear mode of odd (dashed) and even (solid) DCSs vs the coupling constant. Inset: dynamics of a purely oscillating soliton solution. ($E=21, \Delta_1=-4.9, \Delta_2=-23, \delta=0.4$.)

to larger PW amplitudes $|b_1|$ and large negative cavity detuning (Fig. 8).

VI. STABILITY OF BRIGHT DISCRETE SOLITONS

After having found "odd" and "even" bright DCSs we probe these solutions against their stability as it depends on the coupling constant C_1. To this end the usual linear stability analysis has been performed. Using $\overline{u_n}=\overline{U_n}+\overline{a_n}e^{\lambda T}$ we linearize the governing equation (6) around small perturbations $\overline{a_n}=(a_{1n},a_{2n},a_{1n}^*,a_{2n}^*)$ of the stationary solution $\overline{U_n}=(U_n,V_n,U_n^*,V_n^*)$. To disclose the main stability properties of odd and even DCSs it is convenient to select bright DCSs in domains *C* and *D* (similar to profiles shown in Figs. 4 and 5).

In the anticontinuous limit ($C_1=0$) the stability is determined by the stability in a single cavity and does not depend on the DCS symmetry. The DCS has eight eigenvalues for $C_1=0$ which are pairwise complex conjugated. Half of them belong to the PW background and the rest corresponds to the up-switched high-level cavity state in the soliton center. To give specific examples we concentrate on a parameter set, for which all these eigenvalues have the same real part, namely, $\mathrm{Re}\,\lambda=-1$; thus $\lambda=-1\pm i\omega$. This condition is well satisfied in a wide range of the PW hysteresis loop, provided that photon lifetimes are equal for FF and SH fields ($\delta=1$).

First of all we are interested in the mechanism of destabilization of the even DCS for some critical coupling strength. The evolution of the imaginary part of the even soliton eigenvalues ω is sketched in Fig. 10 for our particular example. Here $\omega_h=1.264$ and $\omega_l=0.951$ describe the high- and low-level cavity states corresponding to the case of vanishing coupling. However, the eigenvalue degeneracy disappears with increasing coupling strength. Thus the low-power-state eigenvalue ω_l splits into a continuous band (Fig. 10). By contrast, the high-power-state eigenmode ω_h splits into two eigenmodes, namely, into a symmetric $\overline{A}_{\mathrm{sym}}=(\ldots,0,\overline{a},\overline{a},0,\ldots)$ and an antisymmetric $\overline{A}_{\mathrm{sym}}=(\ldots,0,\overline{a},-\overline{a},0,\ldots)$ one. These eigenmodes are well localized around the soliton center provided that the coupling constant is still small. Therefore their imaginary parts can be approximately described by the following quadratic equations for ω^2:

$$\omega^4+\omega^2[|V_0|^2-4|U_0|^2-(\Delta_1'^2+\Delta_2^2)]+4|U_0|^2(|U_0|^2-\Delta_1'\Delta_2) \\ -|V_0|^2\Delta_2^2+\Delta_1'^2\Delta_2^2=0, \tag{26}$$

where Δ_1' corresponds to $\Delta_1'=\Delta_1-C_1$ for the symmetric and $\Delta_1'=\Delta_1-3C_1$ for the antisymmetric modes. U_0 and V_0 are the field amplitudes in the DCS center. Equation (26) has two independent zeros with respect to ω^2. Here we only consider the solution with the lower value of ω^2, because only this one will finally destabilize. Assuming that the fundamental field amplitude in the DCS center depends linearly on the coupling constant C_1 and solving Eq. (26) we find the eigenvalue of the antisymmetric linear mode of the even DCS for small coupling (see analytical curves in Fig. 10). First, Eq. (26) has real-valued solutions and the corresponding two antisymmetric eigenvalues $\lambda_{\mathrm{asym}}^{\pm}=-1\pm i\omega_{\mathrm{asym}}$ are stable (see Fig. 10). But, for increasing coupling ω^2 becomes negative and therefore the solutions of Eq. (26) become imaginary thus compensating for the negative real part of the eigenvalue. Finally the even DCS loses stability for increasing coupling (see inset of Fig. 10). Obviously, for stronger coupling the considered eigenmodes spread out to several cavities and the approximation (26) is no longer valid.

Direct numerical calculations show that the eigenvalue of the antisymmetric eigenmode finally converges exponentially to zero for increasing coupling constant. This mode transforms to the so-called translational mode (see solid line in Fig. 11) known in continuous models with translational symmetry [32]. The analytical analysis of the eigenmodes of odd DCSs is more involved. The antisymmetric mode bifurcates in our example from the plane $\mathrm{Re}\,\lambda=-1$ as well but unlike the even DCS, it does not lead to soliton instability. This mode also converges to the quasitranslational mode and, therefore, its eigenvalue converges to zero for large coupling constant as well (see dashed line for large coupling in Fig. 11).

There is one more interesting eigenmode of the DCS, which is more prominent for odd DCSs. This mode appears due to the interactions of a localized eigenmode with the continuous spectrum of the soliton background and its eigenvalue possesses an imaginary part (dashed line around $C_1=10$ in Fig. 11). The existence of an oscillating linear mode of a localized discrete solution potentially opens the possibility to find breathing DCSs in arrays of coupled quadratic nonlinear cavities. Indeed, we observed oscillating solutions. Such a purely oscillating soliton solution was recently found in arrays with the Kerr nonlinearity [31]. Unlike in the Kerr case we found oscillating solitons only for relatively large SH detuning Δ_2 (inset in Fig. 11). In this case the mean-field model is valid only for very high-Q cavities.

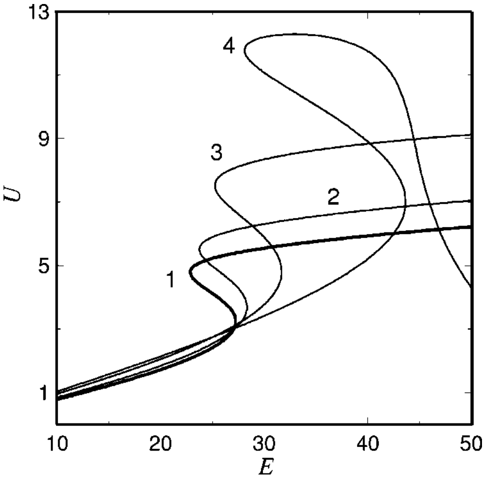

FIG. 13. The intracavity field amplitude at the output mirror for PW solution vs the driving amplitude E in the mean-field approximation (curve 1) and for the round-trip model for $\rho_F=0.95, l=4.9 l_{\rm nl}$ (curve 2); $\rho_F=0.92, l=7.72 l_{\rm nl}$ (curve 3); $\rho_F=0.9, l=9.55 l_{\rm nl}$ (curve 4). Parameters: $\Delta_1=-12.9, \Delta_2=-2, \delta=0.6$.

VII. VALIDITY OF MEAN-FIELD APPROACH

All results presented in the previous parts of this paper were obtained by solving the mean-field model derived in Sec. II. We are now going to compare these predictions with numerical solutions of the complete round-trip model. Before starting we should remember the assumptions that were made to obtain the mean-field equations. The cavity was assumed to be doubly resonant, exhibiting high finesse at both FW and SH frequencies [13,24]. To achieve this goal the reflection coefficients of all mirrors should be close to unity $|1-\rho_{F,S}|\ll 1$. In addition, the effective cavity length should be small enough that coupling, walk-off, mismatch, and frequency conversion have an effect only after many round trips. To reveal the range of validity of the mean-field model we solved numerically the system of forward and backward waves (1) with appropriate boundary conditions (2) for different values of cavity parameters, such as reflectivity, detuning, and effective length. For comparison we give all values in units of the mean-field model [see Eqs. (6) and (7)]. However, even if we fix the parameters of the scaled mean-field approach there are still degrees of freedom left in determining the parameters of the round-trip model. Here we used different values of the cavity length l and of the mirror reflectivity $\rho_{F,S}$, but kept the photon lifetime $\tau_{\rm ph}\approx 2l/\tilde{V}_F(1-\rho_F^2)$ constant. The resonator length is expressed in effective nonlinear lengths $l_{\rm nl}=1/\sqrt{P_F P_S}\chi_{\rm eff}^{(2)}$ where $P_{F,S}$ is the corresponding guide power.

First, we determined the range of bistability of PW solutions derived from both models (Fig. 12). As was expected the discrepancy between both models increases for large detuning and increasing transmissivity $T_{F,S}=1-\rho_{F,S}^2$ of the mirrors (Fig. 12). If the reflectivity is large enough $(1>\rho_{F,S}>0.98)$, the results of the mean-field model coincide almost exactly with the round-trip one, even for large cavity detun-

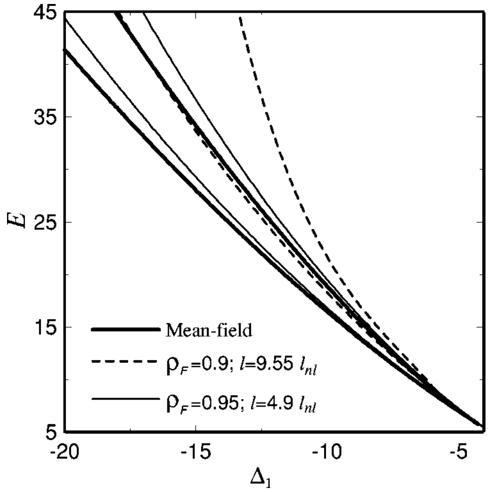

FIG. 12. The boundary of PW bistability domain for different mirror reflectivities and in the mean-field model $(\Delta_2=-2, \delta=0.6)$.

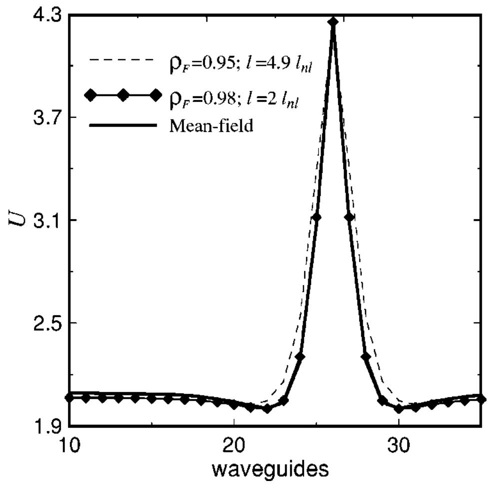

FIG. 14. Intracavity field amplitude profiles of bright solitons for different round-trip parameters $(C_1=5, \Delta_1=-6, \Delta_2=-2, \delta=0.6)$.

ing ($|\Delta_1| < 20$). Although for a relative large negative cavity detuning the mean-field model predictions are not exact even for $\rho_F \approx 0.95$, there is still a good qualitative agreement. There are appreciable quantitative discrepancies for $\rho_F \approx 0.9$ (line 4 in Fig. 13). This involved behavior of low-Q cavities can be understood by accounting for the large frequency conversion upon one passage.

To investigate the validity of the mean-field model for non-PW solutions bright DCSs for different round-trip parameters have been calculated (Fig. 14). It is evident that also in this case the mean-field model holds down to mirror reflectivities of 0.95. Going further it turns out that the mean-field model gives qualitatively correct solutions provided that the reflectivity exceeds 0.92.

VIII. CONCLUSION

In conclusion, we have investigated the optical response of a chain of identical coupled cavities endowed with a quadratically nonlinear material. Starting from a round-trip model we have derived mean-field equations and have checked their validity. On the basis of this mean-field approach we have characterized stationary solutions of the discrete dissipative nonlinear system by means of asymptotic methods. Solving a linearized version of the original equations allowed for an almost exact description of the soliton tails and thus for the identification of domains in parameter space where discrete cavity solitons of different topology may exist. A simple analytical formula was obtained for evaluation of the effective soliton width. Based on these analytical studies we found by numerical means bright DCSs with evanescent as well as oscillating tails and dark staggered DCSs. All these soliton branches emanate subcritically from the bifurcation point. Based on a linear stability analysis of bright DCSs it was shown that even DCSs destabilize due to the action of an antisymmetric eigenmode, which transforms into the translational mode in the quasicontinuous limit (strong coupling).

[1] F. Lederer, S. Darmanyan, and A. Kobyakov, in *Spatial Optical Solitons*, edited by S. Trillo and W. E. Torruellas, Springer Series in Optical Sciences Vol. 82 (Springer-Verlag, New York, 2001), pp. 269–292.

[2] H. S. Eisenberg, Y. Silberberg, R. Morandotti, and J. S. Aitchison, Phys. Rev. Lett. **85**, 1863 (2000).

[3] R. Morandotti, H. S. Eisenberg, Y. Silberberg, M. Sorel, and J. S. Aitchison, Phys. Rev. Lett. **86**, 3296 (2001).

[4] T. Pertsch, T. Zentgraf, U. Peschel, A. Bräuer, and F. Lederer, Phys. Rev. Lett. **88**, 093901 (2002).

[5] T. Pertsch, T. Zentgraf, U. Peschel, A. Bräuer, and F. Lederer, Appl. Phys. Lett. **80**, 3247 (2002).

[6] D. N. Christodoulides, and R. I. Joseph, Opt. Lett. **13**, 794 (1988).

[7] T. Peschel, U. Peschel, and F. Lederer, Phys. Rev. E **57**, 1127 (1998).

[8] S. Darmanyan, A. Kobyakov, and F. Lederer, Phys. Rev. E **57**, 2344 (1998).

[9] A. Kobyakov, S. Darmanyan, T. Pertsch, and F. Lederer, J. Opt. Soc. Am. B **16**, 1737 (1999).

[10] H. S. Eisenberg, Y. Silberberg, R. Morandotti, A. R. Boyd, and J. S. Aitchison, Phys. Rev. Lett. **81**, 3383 (1998).

[11] R. Iwanow, R. Schiek, G. I. Stegeman, T. Pertsch, F. Lederer, Y. Min, and W. Sohler, Phys. Rev. Lett. **93**, 113902 (2004).

[12] R. Reinisch, E. Popov, and M. Neviere, Opt. Lett. **20**, 854 (1995).

[13] L. A. Lugiato and R. Lefever, Phys. Rev. Lett. **58**, 2209 (1987).

[14] D. Michaelis, U. Peschel, and F. Lederer, Phys. Rev. A **56**, R3366 (1997).

[15] V. B. Taranenko, C. O. Weiss, and B. Schäpers, Phys. Rev. A **65**, 013812 (2001).

[16] C. Etrich, U. Peschel, and F. Lederer, Phys. Rev. E **56**, 4803 (1997).

[17] G. L. Oppo, M. Brambilla, and L. A. Lugiato, Phys. Rev. A **49**, 2028 (1994).

[18] U. Peschel, D. Michaelis, and C. O. Weiss, IEEE J. Quantum Electron. **39**, 51 (2003).

[19] W. J. Firth and A. J. Scroggie, Phys. Rev. Lett. **76**, 1623 (1996).

[20] S. Barland, J. R. Tredicce, M. Brambilla, L. A. Lugiato, S. Balle, M. Giudici, T. Maggipinto, L. Spinelli, G. Tissoni, T. Knödl, M. Miller, and R. Jäger, Nature (London) **419**, 699 (2002).

[21] M. Brambilla, L. A. Lugiato, F. Prati, L. Spinelli, and W. J. Firth, Phys. Rev. Lett. **79**, 2042 (1997).

[22] W. J. Firth, G. K. Harkness, A. Lorg, J. M. McSloy, D. Gomila, and P. Colet, J. Opt. Soc. Am. B **19**, 747 (2002).

[23] C. Etrich, U. Peschel, and F. Lederer, Phys. Rev. Lett. **79**, 2454 (1997).

[24] D. Michaelis, U. Peschel, C. Etrich, and F. Lederer, IEEE J. Quantum Electron. **39**, 255 (2003).

[25] S. Trillo and M. Haelterman, Opt. Lett. **23**, 1514 (1998).

[26] D. V. Skryabin, Phys. Rev. E **60**, R3508 (1999).

[27] C. Etrich, D. Michaelis, and F. Lederer, J. Opt. Soc. Am. B **19**, 792 (2002).

[28] R. Kuszelewicz, I. Ganne, I. Sagnes, G. Slekys, and M. Brambilla, Appl. Phys. Lett. **84**, 6006 (2000).

[29] V. B. Taranenko, I. Ganne, R. Kuszelewicz, and C. O. Weiss, Appl. Phys. B: Lasers Opt. **72**, 377 (2001).

[30] V. B. Taranenko, C. O. Weiss, and W. Stolz, Opt. Lett. **26**, 1574 (2001).

[31] U. Peschel, O. Egorov, and F. Lederer, Opt. Lett. **29**, 1909 (2004).

[32] D. Michaelis, U. Peschel, F. Lederer, D. V. Skryabin, and W. J. Firth, Phys. Rev. E **63**, 066602 (2001).